

Simultaneous two-color snapshot view on ultrafast charge and spin dynamics in a Fe-Cu-Ni tri-layer

Benedikt Rösner,^{1*} Boris Vodungbo,² Valentin Chardonnet,² Florian Döring,¹ Vitaliy A. Guzenko,¹ Marcel Hennes,² Armin Kleibert,¹ Maxime Lebugle,¹ Jan Lüning,² Nicola Mahne,³ Aladine Merhe,² Denys Naumenko,³ Ivaylo P. Nikolov,³ Ignacio Lopez-Quintas,³ Emanuele Pedersoli,³ Primož R. Ribič,^{3,4} Tatiana Savchenko,¹ Benjamin Watts,¹ Marco Zangrando,³ Flavio Capotondi,³ Christian David¹, Emmanuelle Jal²

¹ Paul Scherrer Institut, 5232 Villigen PSI, Switzerland

² Sorbonne Université, CNRS, Laboratoire de Chimie Physique – Matière et Rayonnement, LCPMR, 75005 Paris, France

³ Elettra-Sincrotrone Trieste, Strada Statale 14-km 163,5, 34149 Basovizza, Trieste, Italy

⁴ Laboratory of Quantum Optics, University of Nova Gorica, 5001 Nova Gorica, Slovenia

Abstract:

Ultrafast phenomena on a femtosecond timescale are commonly examined by pump-probe experiments. This implies multiple measurements where the sample under investigation is pumped with a short light pulse and has to be probed with a second pulse at various time delays to follow its dynamics. Recently, the principle of streaking extreme ultraviolet (XUV) pulses in the temporal domain has enabled recording the dynamics of system within a single pulse. However, separate pump-probe experiments at different absorption edges lack a unified timing, when comparing the dynamics in complex systems. Here we report on an experiment using a dedicated optical element

and the two-color emission of the FERMI XUV free-electron laser to follow the charge and spin dynamics in composite materials at two distinct absorption edges, simultaneously. The sample, consisting of ferromagnetic Fe and Ni layers, is pumped by an infrared laser and probed by a two-color XUV pulse with photon energies tuned to the M-shell resonances of these two transition metals. The experiment geometry intrinsically avoids any timing uncertainty between the two elements and unambiguously reveals an approximately 100 fs delay of the magnetic response with respect to the electronic excitation for both Fe and Ni. This delay shows that the electronic and spin degrees of freedom are decoupled during the demagnetization process. We furthermore observe that the electronic dynamics of Ni and Fe show pronounced differences for the two probed photon energies while the demagnetization dynamics are similar. These observations underline the importance of simultaneous investigation of the temporal response of both charge and spin in multi-component materials. In a more general scenario, the experimental approach can be extended to continuous energy ranges, promising the development of jitter-free transient absorption spectroscopy in the XUV and soft X-ray regimes.

The use of extremely short light pulses is a powerful way to investigate ultrafast phenomena occurring on a femtosecond timescale. With the advent of sources that can provide ultrashort XUV and X-ray pulses, such as femtoslicing, high harmonic generation, and XUV/X-ray free-electron lasers (FELs), the study of ultrafast dynamics specific to an element in condensed matter or atomic and molecular systems is possible in pump-probe experiments¹⁻³. In this process, the sample under investigation is excited by a pump pulse and subsequently probed by a second, delayed pulse that is sensitive to the physical effect induced by the excitation. The response of the examined material is followed by varying the time delay between the pump and probe pulses, down to time scales limited by the pulse lengths. This experimental approach, both with

optical and XUV/X-ray radiation, provides an opportunity to follow a wide range of ultra-fast processes involving electrons, spins, phonons or other quasi-particles⁴⁻⁶. However, some unavoidable difficulties arise in such experiments. For instance, timing inaccuracies are induced by the jitter between pump and probe, e.g. due to synchronization errors between different sources or to mechanical instabilities. Furthermore, the initial state of the investigated system has to be fully recovered between the individual exposures to pump and probe pulses. This second aspect limits the potential of ultra-fast, time-resolved experiments severely whenever either the pump or the probe pulses induce irreversible changes, such as static heating that degrades the sample, or the sample recovery time limits the rate at which statics can be acquired.

These limitations have been overcome using the principle of streaking the arrival time of XUV pulses at the interaction area. In this specific optical scheme, a whole time trace of a pump-probe experiment is recorded within a single shot from an FEL source^{7,8}. This is achieved by stretching the incoming XUV pulse with an off-axis Fresnel zone plate, which introduces an angular encoding of its arrival time at the focus that becomes spatially separated in the far field. The time-streaking method has been demonstrated to provide jitter-free access to a time window of several picoseconds at the M-edges of transition metals^{8,9}. This method for time-resolved experiments had previously been restricted to a monochromatic probe beam and so a single shot dynamics measurement with a unified time scale arising from the same pulse could not be applied to multi-element systems until now. This restriction prevented access to electronic and spin dynamics in complex materials where the excitation can flow through different pathways that involve various species during its time evolution, for instance in charge transfer processes, where the electronic wave-packet migrates to a different atomic site.

An increasing number of technologically relevant systems are being composed of multiple elements with a view towards integrating ultrafast magnetism effects into devices. In such composite systems, the

interplay of charge and spin degrees of freedom between the different elements is not yet fully understood¹⁰⁻¹³. For example, tri-layer systems, in which spin currents are generated in an upper ferromagnetic (FM) layer and spread through a non-magnetic (NM) spacer towards a bottom FM layer, have been under intense investigation¹⁴⁻²⁰. In a previous study, the observed enhancement of the magnetization of the bottom layer has been attributed to a superdiffusive current created in the top layer¹⁵. However, this effect has not been observed in other systems^{16,19}, despite a systematic approach to changing the NM layer to investigate methods to control this superdiffusive current. In all of these studies, the electronic and magnetization dynamics of both FM layers have been probed separately, and hence information about the relative dynamics between the two magnetic layers has been limited by jitter. The ability to follow the evolution of XUV/X-ray absorption spectra (XAS), including magnetization using X-ray magnetic circular dichroism (XMCD) effects, simultaneously at multiple absorption edges would provide a unified time scale for the set of FM layers and allow new insight into the microscopic dynamics and interplay of such complex systems.

We have developed a custom optical element that allows us to probe the XUV absorption of a composite material simultaneously at both the iron and nickel M-edge within a time window of 2.7 ps (Figure 1). Using the two-color mode of the FERMI FEL tuned at two different harmonics of the seed laser²¹, a pair of simultaneous probe pulses is focused onto the sample, and its arrival time is streaked onto the detector with a common time axis that is defined by the fixed geometry. Repeating the measurement with opposing sample magnetizations gives access to the charge and magnetic dynamics. This scheme is applied to study an Fe/Cu/Ni tri-layer in which Fe and Ni are ferromagnetically coupled.

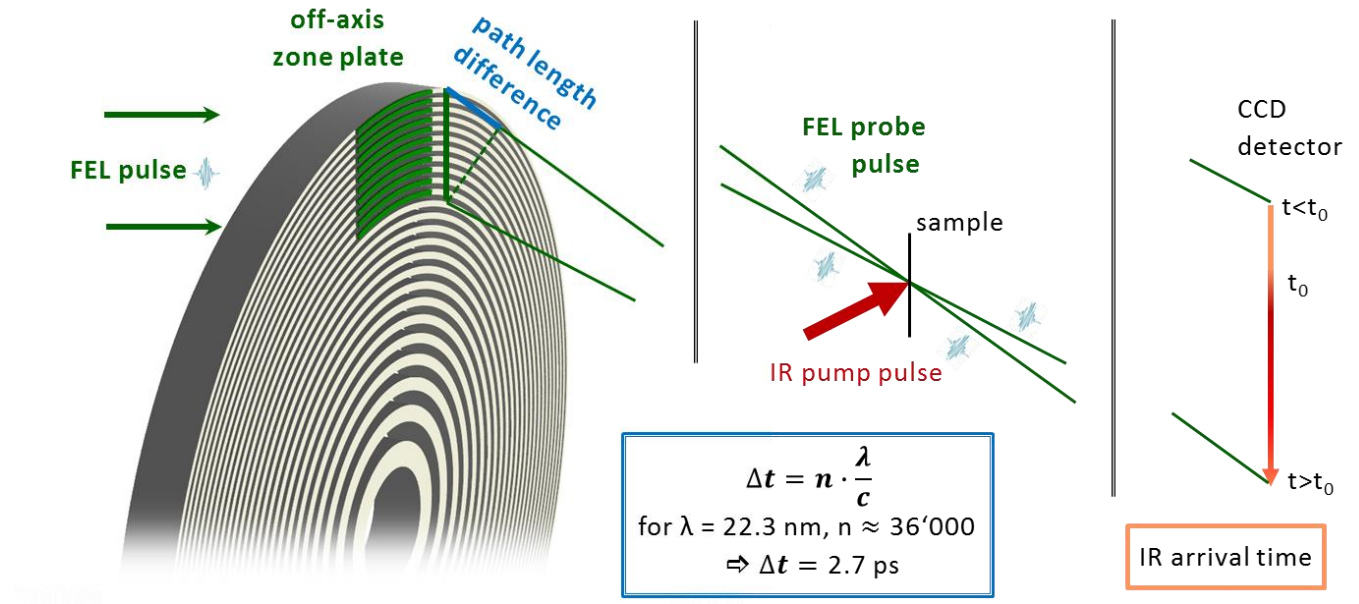


Figure 1 | Illustration of the time-streaking concept. An incoming light pulse is diffracted by an off-axis zone plate, which is the outer area of a Fresnel zone plate lens. Inherent to the condition for first order constructive interference, each zone pair induces an exact path difference of the wavelength of the diffracted light. This path length difference then results in a time delay Δt that is well defined by the speed of light. In this particular example with 36'000 zone pairs and a wavelength of 22.3 nm, the arrival time of the diffracted beam in the focus spot is stretched over a 2.7 ps time window and projected geometrically (i.e. streaked) onto a two-dimensional detector. By pumping the sample at the focus position, 2.7 ps of its dynamics can be recorded by a single light pulse from a free electron laser.

In previous experiments^{8,9}, we focused the FEL beam with an off-axis zone plate to a spot in the sample plane that was also optically pumped (Figure 1 and Figure 2a). However, zone plates have a focal length proportional to the photon energy of the incident light and so a single zone plate cannot focus a two-color beam onto a single spot. We therefore designed the two-color experiment to utilize two adjacent off-axis zone plates that share a common optical axis (i.e. two halves of a single zone pattern) and with zone placement designed to focus their respective photon energies to the same focal plane (Figure 2c). Considering the same displacement from the optical axis and numerical aperture for both cases, two zone plate patterns can be designed for a known energy or wavelength ratio according to:

$$\frac{\Delta r_1}{\Delta r_2} = \frac{E_2}{E_1} = \frac{\lambda_1}{\lambda_2}, \quad (\text{eq. 1})$$

where Δr is the width of the outermost zone.

In order to probe the M-edges of Fe and Ni simultaneously, the electron bunch of the FERMI FEL source was seeded with a single optical laser pulse ($\lambda_{seed} = 245$ nm) and the undulator section was split into two subsections resonant at $\lambda_1 = \lambda_{seed}/m_1$ and $\lambda_2 = \lambda_{seed}/m_2$, where m_1 and m_2 are integer harmonic numbers. We chose the 13th harmonic to access the Ni M-edge at 65.8 eV ($\lambda_{Ni} = 18.8$ nm), and the 11th harmonic for the Fe M-edge at 55.7 eV ($\lambda_{Fe} = 22.2$ nm). According to eq. (1) and a lower limit of 40 nm arising from the nanofabrication process, the ratio of the outermost zone width is given by:

$$\frac{\Delta r_{Fe}}{\Delta r_{Ni}} = \frac{\lambda_{Fe}}{\lambda_{Ni}} = \frac{m_{Ni}}{m_{Fe}} = \frac{13}{11} = \frac{47.3 \text{ nm}}{40.0 \text{ nm}} \quad (\text{eq. 2})$$

Since a binary zone plate does not cause wavelength-dependent phase retardation (and hence different optical path lengths for the two colors), both beams travel through path lengths determined by geometry to be exactly the same distance. Thus, the time window is identical for both colors. Note that each half of the off-axis zone plate will diffract both beam components, and will therefore produce two additional first order focus spots with longer and shorter focal length than the desired overlapping focal plane. However, these parasitic beams are well separated from the two-color focus and can be spatially filtered by the aperture formed by the frame of the sample support.

The previously developed streaking approach recorded the negative, divergent diffraction order on a second camera for an intensity normalization to eliminate the effects of the significant shot-to-shot fluctuations inherent to the incident FEL beam^{8,9}. However, this intensity normalization scheme cannot be extended to the multi-color case since the negative diffraction order of two different wavelengths cannot be separated in space on the reference detector. To address this issue, we combined our two-part, off-axis zone plate with a phase grating that splits the beam perpendicular to the diffraction angle of the off-axis

zone plate. An elegant way to integrate a beam splitter in a diffractive optical element is a periodic inversion of the zone pattern as shown in Figure 2 b), resulting in a twin spot of the off-axis zone plate in the focal plane with a defined separation. In this way, one of these spots can be optically pumped while the other records the sample absorption in the unperturbed state. A consequence of this focus splitting is that the beam paths followed by the two colors is no longer exactly equal, but is slightly shorter for the color coming from the off-axis zone plate half on the same side as the focus. This path length difference presents itself in the detector image as a tilt of the line describing equal time values since the path length difference is minimal at the boundary of the color sections and increases (in the corresponding sense) linearly with the distance from the color boundary (Figure 2c).

The periodicity p of the zone inversion for the beam splitter is chosen in the same ratio as the outermost zone widths in order to achieve the same focus spot displacement for the two colors:

$$\frac{p_{Fe}}{p_{Ni}} = \frac{13}{11} = \frac{709 \text{ nm}}{600 \text{ nm}} \quad (\text{eq. 3})$$

With this set of parameters, we designed off-axis zone plates with an area of 3.8 mm x 3.8 mm, which is part of a virtual zone plate lens with a diameter of $D = 35.0$ mm. The resulting focal length is 74.4 mm, the spot displacement from the optical axis is 2.3 mm. The optical elements were fabricated by etching nanostructures into a 200 nm thick silicon membrane purchased from Norcada, Inc. using a process described elsewhere^{22,23}.

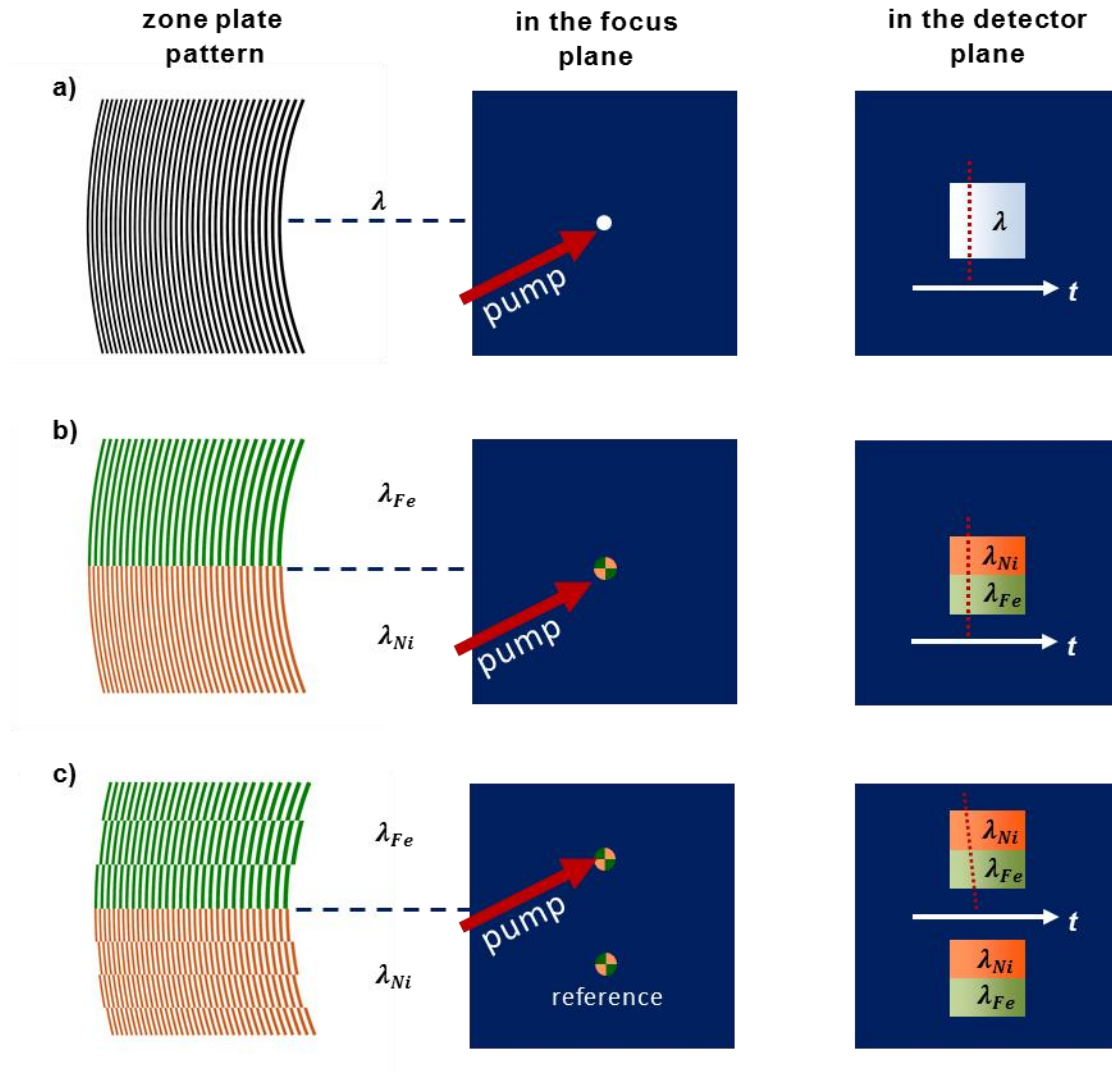


Figure 2 | Twin focus off-axis zone plate for two colors. **a)** Off-axis zone plate as previously used for time-streaking experiments^{8,9}. **b)** Two off-axis zone plate patterns are placed next to each other in a way that a two-color beam with two compound energies is focused onto the same spot. **c)** A beam splitter grating perpendicular to the zones is integrated by periodic inversion of the zone plate patterns. This splits the focus spot into twin copies with defined separation, and introduces a slight tilt to the locus of equal time points in the detector image.

Figure 3a shows the recorded image of a shadow mask test pattern placed upstream of the two-color, twin-focus, off-axis zone plate and attests to its quality by the homogeneous, magnified double-projection of the test pattern onto the detector. Each replica of the shadow mask projection consists of two well-defined

halves, which can be attributed to the two halves of the zone plate pattern and their corresponding photon energies. Note that the intensity of the FEL beam at 55.7 eV ($\lambda_{Fe} = 22.2$ nm) is lower compared to the radiation with higher photon energy ($\lambda_{Ni} = 18.8$ nm), and follows the image brightness in the upper and lower halves of each test pattern image. This is due to the energy-dependent beamline transmission, and more particularly due to the absorption of the 200 nm Al solid-state attenuators that were used to protect the sample from damage. Looking at the edges of the depicted logos, we can see that the lower and upper halves are exactly aligned, indicating that the geometry and thus the timing of the two beams matches. As illustrated in Figure 2c, the projection below the optical axis is used as a reference, while the upper one is used to track the pump-induced absorption changes. Division of one image by the other gives a precise normalization of the incident two-color beam on a shot-to-shot basis (see supplementary material for details).

We investigated a magnetic sample that consists of a tri-layer of polycrystalline metallic films (10 nm Ni, 2 nm Cu, and 10 nm Fe), all grown on top of a 3 nm thin metallic Ta adhesion layer by sputtering. The Ta adhesion layer was deposited directly onto silicon nitride (Si_3N_4) membranes ($200 \times 200 \mu m^2$) of 30 nm thickness. To prevent oxidation, the Ni film was capped with a 3 nm thin Al layer. The detailed structure of the entire stack is shown in Figure 4a. Static magneto-optic Kerr effect measurements confirmed the expected in-plane magnetization of the Ni and Fe films, which are ferromagnetically coupled through the Cu layer. The tri-layer sample was placed in the focal plane of the twin-focus, off-axis zone plates such that one membrane window was brought to the upper focus spot and pumped by the IR laser (780 nm wavelength, 100 fs pulse duration, 2.5 μJ incident pulse energy). Another part of the magnetic layer system was aligned such that the lower focus spot passed through it to obtain an unperturbed reference beam. In this way, the two projections on the detector contain information on the transmitted signal from a pumped sample region, as well as the unpumped reference as described in the previous paragraph. The ratio of these two images yields the transient transmission of the sample when it

is excited. Repeating the measurement with a magnetic field of approximately 130 mT applied in opposite direction allows us to retrieve XAS and XMCD signals from the sum and difference of the measurements, respectively, which are sensitive to the transient changes in the charge and spin states of the magnetic system. For probing the in-plane magnetization, the sample was tilted by 18° with respect to the incident beam. More information on the experimental geometry can be found in the supplemental material.

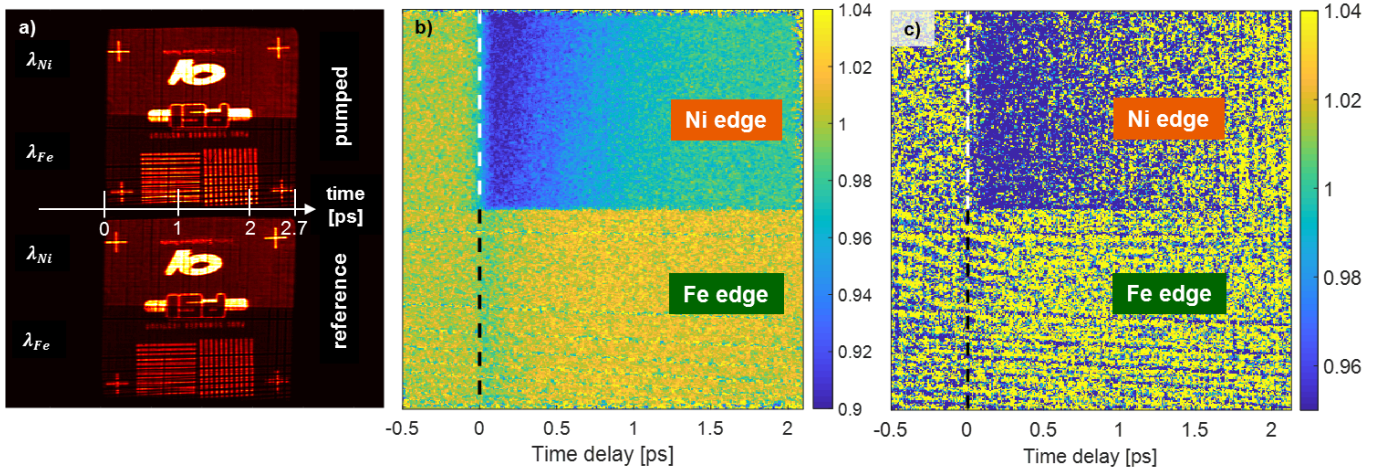


Figure 3 | Time-streaking experiment at two absorption edges. **a**, Projection of a shadow mask placed in front of the zone plate onto the detector. The two color beams are visible as a distinct contrast on the recorded image due to different pulse intensity. The arrival time of the 2-color probe beams is dispersed along the horizontal direction. In the time resolved experiment, one focus spot is pumped with an IR laser while the unpumped one is used as reference. Note that the detector image has been rotated by 180° to the reader's perspective. **b**, Temporal evolution of the transmission of a pumped iron-nickel tri-layer sample after optical excitation (the dashed line identifies $t = 0$) integrated over 600 shots. The upper part corresponds to the Ni M-edge, while the lower part shows the time evolution of the signal at the Fe M-edge. The reported images are normalized and corrected with respect to the zone plate curvature using the same procedure as described by Buzzi *et al.*, and Jal *et al.*^{8,9}, and with respect to the time delay induced by the beam splitter grating. **c**, Respective image recorded with a single FEL pulse exposure.

In order to take into account variations in the local absorption and detector response, the normalized picture has also to be divided by background images taken without the infrared pump. Since the time delay is a function of the zone placement, the curvature of the zone plate has to be corrected as reported before^{8,9}. The resulting picture retrieved for an accumulation of 600 shots is shown in Figure 3b. We would like to emphasize here that it is possible to measure a signal even with one single shot, as shown in Figure 3c. We will, however, concentrate on the data taken for an accumulation of 600 shots in the following as the process we are investigating is fully reversible.

Integration of the two areas with the different photon energies shows the evolution of XUV transmission in time. The logarithm of this normalized signal directly gives the relative absorption $\Delta\mu^+(t)$ and $\Delta\mu^-(t)$ for the two different magnetization directions, corresponding to the difference between the dynamic and static absorption ($\Delta\mu^{+/-}(t) = \Delta\mu^{+/-}(t) - \Delta\mu^{+/-}(t < 0)$, see supplementary material). The average of these two signals shows the time evolution of the absorption, ΔXAS , and the difference gives the change in magnetic contrast with time, $\Delta XMCD$. ΔXAS is sensitive to the transient electronic charge whereas $\Delta XMCD$ is proportional to the transient electronic spin dynamics²⁴. Figure 4b shows the ΔXAS and $\Delta XMCD$ response of the Ni and Fe layers, respectively. We can clearly observe that the spin dynamics for both elements are delayed by approx. 100 fs with respect to the charge response. Moreover, the electronic temporal dependence of the Fe film is strikingly different from that of the Ni film, while the magnetic behavior is similar, as demonstrated by the comparison of ΔXAS and $\Delta XMCD$ of both elements in Figure 4c. While Figure 4b highlights a delay of the XMCD signal with respect to the electronic response, from the comparison in Figure 4c, we can clearly observe that there is no relative delay between the two species (Fe and Ni). To our knowledge, this is the first time that a delay in the spin degree of freedom with respect to an excitation in the electronic system is observed in ferromagnetic elements, although such delay has been predicted theoretically by Zhang *et al.*^{25,26}. Other measurements performed on a completely different system (that will be presented and discussed in a future publication) seem to

indicate that the observed delay is specific to the M-edge excitation and depends on the probing photon energies. This would explain why earlier time-resolved XAS and XMCD studies, which have been performed at the L₃-edge of the 3d transition metals, have not observed a delayed onset of the electronic and magnetic dynamics^{27,28}.

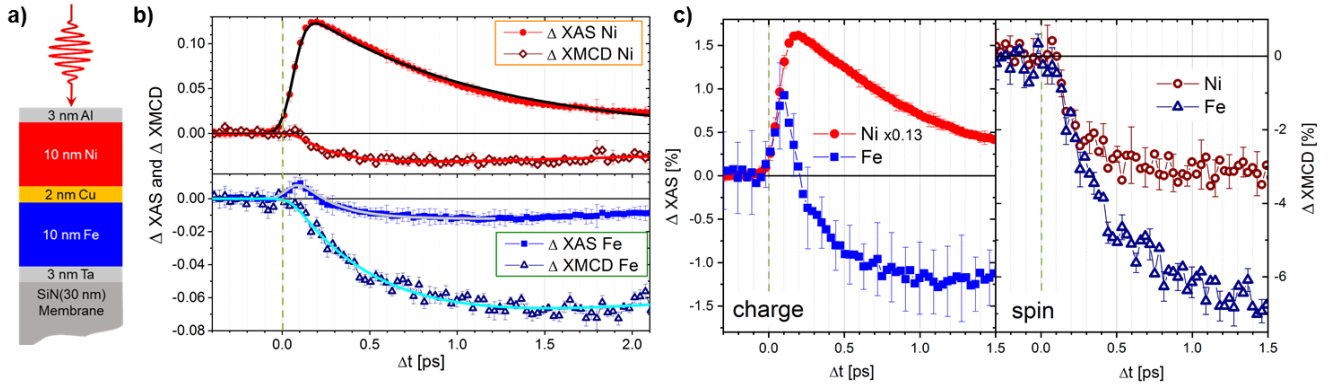


Figure 4 | Jitter-free charge and spin dynamics of iron and nickel probed simultaneously with the same absolute timing. **a**, Layer structure of the investigated tri-layer film. **b**, Time traces for nickel (red, upper part) and iron (blue, lower part). The average signal of the traces recorded at opposite magnetic field gives the transient XUV absorption ΔXAS and thus a measure for the charge dynamics (solid symbols), whereas the difference of these two signals gives the $\Delta XMCD$ signal that represents the spin dynamics (open symbols). **c**, The direct comparison of ΔXAS and $\Delta XMCD$ for Ni and Fe shows that the charge dynamics (left hand side) begin sooner than the spin dynamics (right hand side). Note that the ΔXAS curve for Ni has been scaled down for better comparability. t_0 is marked with a dashed line.

Although this delay between $\Delta XMCD$ and ΔXAS is not observed in previous experiments at the L₃-edge, we note that the marked dynamics we measured here for ΔXAS of Ni is very similar to the one measured by Stamm *et al.*²⁷ and predicted by Carva *et al.*²⁹ at the L₃-edge of Ni. According to the latter work, these dynamics arise from a change of the electron density of states induced by the IR pump. Since the M-edge is wider than the L₃-edges and since we are not probing on the flat top part of the Ni absorption edge (\approx

67 eV) but at slightly lower photon energy (65.8 eV), i.e. on the steep slope of the absorption spectrum (Figure 5a), we are very sensitive to the change of electronic density of states. In our case, most of the IR photons are absorbed by valence electrons during the excitation of the sample, and Ni valence electrons that lie 1.5 eV below the Fermi level are promoted into empty states above it. As pointed out by Carva *et al.* in their simulations²⁹, this process will generate hot electrons that cannot be modeled by a Fermi-Dirac distribution, and will produce a dynamical shift of the XAS spectrum towards lower energies, increasing the sample absorption for photons below the resonance energy on ultrashort time scales. On longer time scales, the excited electrons relax and fill the empty states in the valence band, thereby reducing the number of available transitions for the XUV absorption events at photon energies below the resonance condition. In order to extract characteristic times from our data, all curves have been fitted by a two exponential model¹⁴ to extract the typical time constants. The fits are shown in Figure 4b, and the fit parameters are given in the supplemental material and discussed in the next paragraphs. The double exponential fit shown in Figure 4a yields a rise time constant of 38 fs with a decay time constant of 1 ps, in good agreement with the lifetime of optically excited electrons in Ni³⁰⁻³².

If we apply the same reasoning for Fe, the 1.5 eV excitation will lead to an initial increase of the transient XUV absorption and a subsequent decrease already underway before the onset of the slower relaxation process. This is because the probing energy is closer to the absorption peak (55.7 eV, Figure 5a), which shifted to lower photon energies during the excitation process. These dynamics are indeed observed in our experiments as demonstrated in Figure 4b. The double exponential fit in Figure 4b yields a rising time constant of 30 fs – well below the energy resolution of the experimental setup – for Fe, and a time constant of 200 fs for its decrease.

At first glance, the magnetic dynamics observed for both Fe and Ni seem more usual since they show a classical ultrafast demagnetization behavior. However, the Ni layer has a demagnetization time constant

of 240 fs while the Fe layer has a constant of 500 fs. Compared to previous results in the literature^{27,33,34}, our data shows a demagnetization that is slightly slower for Ni and more than twice as slow as usually observed for Fe. This can also be explained by the fact that we are not probing exactly at the element-specific resonances, which are at 54.2 eV for Fe and 66.2 eV for Ni, but 1.5 eV above the Fe M-edge and 0.4 eV below the Ni M-edge. Indeed, a recent paper by Gort *et al.*³⁵ points out that the observed dynamical behavior of the spin polarization depends not only on time but also on the binding energy of the probed electrons with respect to the Fermi level. The slower demagnetization time for Fe could furthermore be due to a possible pure spin current travelling between Ni and Fe at a longer time scale^{36,37}. Within a simple band model as shown in Figure 5b, a unidirectional transfer of Ni minority electrons into the Fe minority band can be possible. If we consider the band structure of Fe and Ni, there are mainly d-states available up to 1.5 eV above the Fermi level in Fe, while Ni possesses only s-states (Figure 5b). This implies that the excited electrons are almost completely in the localized 3d band in Fe, while they are in the itinerant 4s band in Ni. Thus, excited electrons in Ni can flow across the Cu layer, and fill the empty states of the minority band of Fe, leading to a decrease in the overall magnetization of Fe in addition to the intrinsic laser-induced demagnetization. Although the limited thickness of our tri-layer system implies that all magnetic layers are optically excited (the Ni layer absorbs 10.6% of the incoming IR fluence while the Fe layer absorbs 12.2%, see supplementary material for the complete IR absorption profile), it seems that there is no transport of the Fe excited electrons into the Ni. This is mainly because the excited Fe electrons are localized in the d-states available up to 1.5 eV above the Fermi level.

Finally, we would like to point out that the spin transport proposed above is different from the consequence of an optically induced spin and orbital momentum transfer occurring in the first few femtoseconds, described recently by Siegrist *et al.*³⁸. In our case, the spin transport occurs on longer timescales and over more than 2 nm of Cu. We therefore hope our results will encourage new theoretical simulations to

understand the interplay of electron dynamics in coupled 3d metals over a time range of several hundreds of femtoseconds in detail.

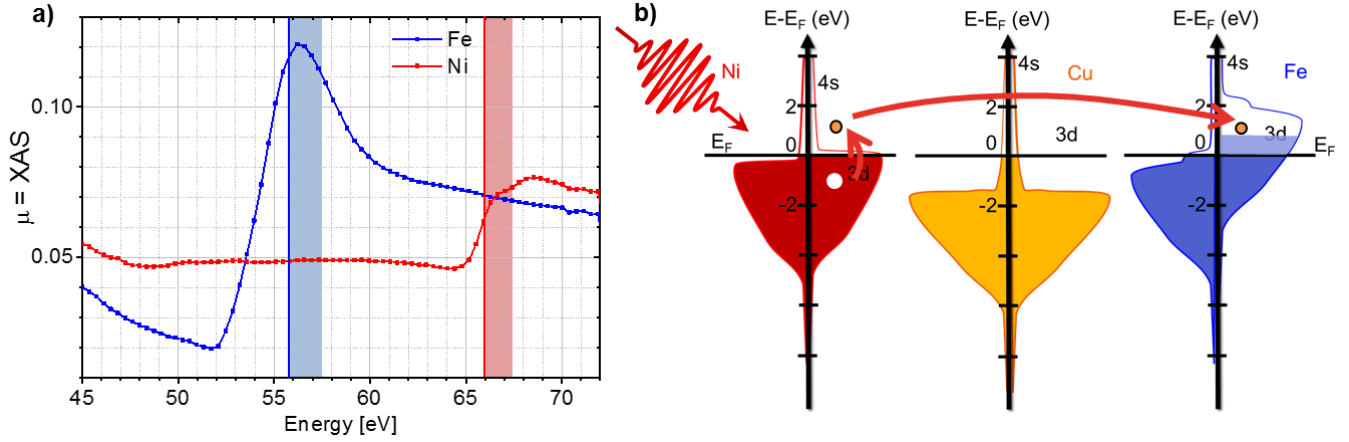


Figure 5 | Microscopic model for the observed data. **a**, Static absorption as reported by Willems *et al.*²¹. The vertical lines indicate the probed energies while the shaded areas indicate the 1.5 eV excitation by the IR laser. **b**, Simplified density of states of Ni, Cu and Fe, adapted from Zhukov *et al.*^{31,39}. The empty states in Ni are mostly itinerant s-states whereas mostly localized d-states are present in Fe. This implies that excited Ni electrons are mainly itinerant and can travel through the Cu layer (red arrow) to fill the empty states of the Fe minority band (light blue area), reducing the Fe magnetization further.

Our results demonstrate that it is possible to investigate the dynamics of a multicomponent system at two discrete photon energies with absolute timing. The special benefit of this method arises from the new normalization scheme based on a beam splitter grating that is directly integrated into the off-axis zone plate used for the time-streaking method^{8,9}. In this way, it is not only possible to conduct an entire pump-probe experiment in a single snapshot, but also to design parts of the zone plate for discrete energies in a fixed geometry, and thus to maintain a uniform time scale across the dynamics of multiple elements. To the best of our knowledge, this is the first time that all these advantages have been combined in the XUV regime.

By investigation of magnetism in the femtosecond regime, this study shows the potential, and the necessity, of simultaneously probing spin and charge in heterostructures. This multi-parameter approach leads to valuable new insights into the existing theory and to a more comprehensive understanding of the microscopic mechanisms that are responsible for ultrafast electronic processes. Our two-color XUV streaking experiment has, for instance, the potential to resolve the controversy of small time delays in the onset of demagnetization of Fe and Ni sublattices^{34,40}.

Taking a step even further, the extension of this method to continuous energies opens up perspectives for single-shot transient spectroscopy in the XUV and soft X-ray regime, in particular at facilities that offer ultrashort and large bandwidth pulses. The present approach divides the zone plate pattern into two halves that are designed for two discrete energies. However, modifying the zone plate pattern with a smooth transition of the zone spacing would allow for the focusing of a continuous spectrum onto the same spot. Figure 6a shows such a possible design with an integrated beam splitter that focuses a spectrum with 7% bandwidth to two discrete spots by modification of the zone plate equation in the vertical direction (keeping the focal distance constant) and a continuous increase in the inversion period. In order to avoid diffraction of the light at different angles outside of the desired focus spot (*i.e.* the parasitic focus spots), such an optical element will require illumination with a matched energy chirp. This is ideally suited to new large-bandwidth operation schemes such as provided at SwissFEL⁴¹. Potential applications for this experimental scheme are time-resolved experiments at the carbon K-edge between 280 and 300 eV. Figure 6b shows an artist's impression of the potential data coming out of such an experiment with a realistically attainable bandwidth of 7%, whereas the time window can extend to approx. half a picosecond at these wavelengths. This paves the way towards real femtosecond single-shot transient spectroscopy conducted at X-ray free electron laser facilities.

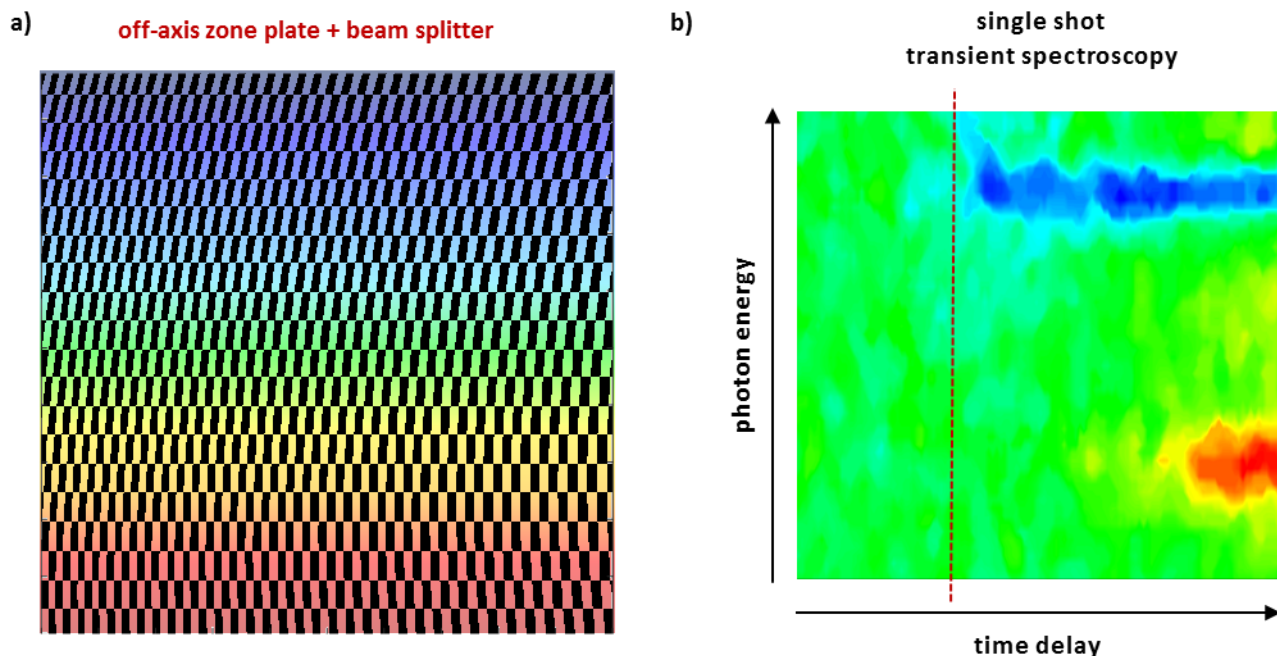


Figure 6 | Schematic illustration of a spectroscopic time-streaking experiment. **a**, Geometry of an off-axis zone plate with integrated beam splitter with a continuous variation of the zone plate pattern to maintain the same focal length over an energy window of 7%. **b**, Artist's impression of a potential data set coming from such a transient spectroscopy experiment. An energy spread of 7% is sufficient to cover, for instance, the near-edge resonances at the carbon K-edge between 280 and 300 eV with a time window of 0.5 ps.

Acknowledgements

This work was funded within the EU-H2020 Research and Innovation Programme, No. 654360 NFFA-Europe (BR) and No. 737093 FEMTOTERABYTE. The authors are grateful for financial support received from the CNRS-MOMENTUM, the SNSF project (No. 200021_160186), the UMAMI ANR-15-CE24-0009, and the CNRS-PICS programs. Access to Synchrotron SOLEIL and beamline SEXTANTS through proposal ID 20160880 for characterization of static properties of the tri-layers is acknowledged. We also thank Clemens von Korff Schmising and Peter Oppeneer for stimulating discussion.

Data Availability

The datasets of the 2-color time-streaking experiment as recorded by the camera are available under the Creative Common license in the Zenodo repository, <https://doi.org/10.5281/zenodo.3735723>.

References

- 1 Beye, M., Sorgenfrei, F., Schlotter, W. F., Wurth, W. & Föhlisch, A. The liquid-liquid phase transition in silicon revealed by snapshots of valence electrons. *P. Natl. Acad. Sci. USA* **107**, 16772, doi:<https://doi.org/10.1073/pnas.1006499107> (2010).
- 2 Squibb, R. J. *et al.* Acetylacetone photodynamics at a seeded free-electron laser. *Nat. Commun.* **9**, 63, doi:<https://doi.org/10.1038/s41467-017-02478-0> (2018).
- 3 Smallwood, C. L. *et al.* Tracking Cooper Pairs in a Cuprate Superconductor by Ultrafast Angle-Resolved Photoemission. *Science* **336**, 1137, doi:<https://doi.org/10.1126/science.1217423> (2012).
- 4 Beaurepaire, E., Merle, J. C., Daunois, A. & Bigot, J. Y. Ultrafast Spin Dynamics in Ferromagnetic Nickel. *Phys. Rev. Lett.* **76**, 4250-4253, doi:<https://doi.org/10.1103/PhysRevLett.76.4250> (1996).
- 5 Bencivenga, F. *et al.* Four-wave mixing experiments with extreme ultraviolet transient gratings. *Nature* **520**, 205, doi:<https://doi.org/10.1038/nature14341> (2015).
- 6 Fausti, D. *et al.* Light-Induced Superconductivity in a Stripe-Ordered Cuprate. *Science* **331**, 189, doi:<https://doi.org/10.1126/science.1197294> (2011).
- 7 David, C. *et al.* Following the dynamics of matter with femtosecond precision using the X-ray streaking method. *Sci. Rep.* **5**, 7644, doi:<http://dx.doi.org/10.1038/srep07644> (2015).
- 8 Buzzi, M. *et al.* Single-shot Monitoring of Ultrafast Processes via X-ray Streaking at a Free Electron Laser. *Sci. Rep.* **7**, 7253, doi:<https://dx.doi.org/10.1038/s41598-017-07069-z> (2017).
- 9 Jal, E. *et al.* Single-shot time-resolved magnetic x-ray absorption at a free-electron laser. *Phys. Rev. B* **99**, 144305, doi:<https://doi.org/10.1103/PhysRevB.99.144305> (2019).
- 10 Graves, C. E. *et al.* Nanoscale spin reversal by non-local angular momentum transfer following ultrafast laser excitation in ferrimagnetic GdFeCo. *Nat. Mater.* **12**, 293, doi:<https://doi.org/10.1038/nmat3597> (2013).
- 11 Iacocca, E. *et al.* Spin-current-mediated rapid magnon localisation and coalescence after ultrafast optical pumping of ferrimagnetic alloys. *Nat. Commun.* **10**, 1756, doi:<https://doi.org/10.1038/s41467-019-09577-0> (2019).
- 12 Granitzka, P. W. *et al.* Magnetic Switching in Granular FePt Layers Promoted by Near-Field Laser Enhancement. *Nano Lett.* **17**, 2426-2432, doi:<https://doi.org/10.1021/acs.nanolett.7b00052> (2017).
- 13 Ferrari, E. *et al.* Widely tunable two-colour seeded free-electron laser source for resonant-pump resonant-probe magnetic scattering. *Nat. Commun.* **7**, 10343, doi:<https://doi.org/10.1038/ncomms10343> (2016).
- 14 Malinowski, G. *et al.* Control of speed and efficiency of ultrafast demagnetization by direct transfer of spin angular momentum. *Nat. Phys.* **4**, 855-858, doi:<https://doi.org/10.1038/nphys1092> (2008).

- 15 Rudolf, D. *et al.* Ultrafast magnetization enhancement in metallic multilayers driven by superdiffusive spin current. *Nature Commun.* **3**, 1037, doi:<https://doi.org/10.1038/ncomms2029> (2012).
- 16 Turgut, E. *et al.* Controlling the Competition between Optically Induced Ultrafast Spin-Flip Scattering and Spin Transport in Magnetic Multilayers. *Phys. Rev. Lett.* **110**, 197201, doi:<https://doi.org/10.1103/PhysRevLett.110.197201> (2013).
- 17 Schellekens, A. J., de Vries, N., Lucassen, J. & Koopmans, B. Exploring laser-induced interlayer spin transfer by an all-optical method. *Phys. Rev. B* **90**, 104429, doi:<https://doi.org/10.1103/PhysRevB.90.104429> (2014).
- 18 Choi, G.-M., Min, B.-C., Lee, K.-J. & Cahill, D. G. Spin current generated by thermally driven ultrafast demagnetization. *Nat. Commun.* **5**, 4334, doi:<https://doi.org/10.1038/ncomms5334> (2014).
- 19 Alekhin, A. *et al.* Femtosecond Spin Current Pulses Generated by the Nonthermal Spin-Dependent Seebeck Effect and Interacting with Ferromagnets in Spin Valves. *Phys. Rev. Lett.* **119**, 017202, doi:<https://doi.org/10.1103/PhysRevLett.119.017202> (2017).
- 20 Eschenlohr, A. *et al.* Spin currents during ultrafast demagnetization of ferromagnetic bilayers. *J. Phys. Condens. Matter* **29**, 384002, doi:10.1088/1361-648x/aa7dd3 (2017).
- 21 Willems, F. *et al.* Multi-color imaging of magnetic Co/Pt heterostructures. *Struct. Dynam.* **4**, 014301, doi:<https://doi.org/10.1063/1.4976004> (2017).
- 22 Rösner, B. *et al.* High resolution beam profiling of X-ray free electron laser radiation by polymer imprint development. *Opt. Express* **25**, 30686-30695, doi:<https://doi.org/10.1364/OE.25.030686> (2017).
- 23 Ribič, P. R. *et al.* Extreme-Ultraviolet Vortices from a Free-Electron Laser. *Phys. Rev. X* **7**, 031036, doi:<https://doi.org/10.1103/PhysRevX.7.031036> (2017).
- 24 Stöhr, J. & Siegmann, H. C. *Magnetism*. Vol. 152 (Springer-Verlag, 2006).
- 25 Zhang, G. P., Bai, Y. H., Jenkins, T. & George, T. F. Laser-induced ultrafast transport and demagnetization at the earliest time: first-principles and real-time investigation. *J. Phys. Condens. Matter* **30**, 465801, doi:<https://doi.org/10.1088/1361-648x/aae5a9> (2018).
- 26 Zhang, G. P., Hübner, W., Lefkidis, G., Bai, Y. & George, T. F. Paradigm of the time-resolved magneto-optical Kerr effect for femtosecond magnetism. *Nat. Phys.* **5**, 499-502, doi:<https://doi.org/10.1038/nphys1315> (2009).
- 27 Stamm, C. *et al.* Femtosecond modification of electron localization and transfer of angular momentum in nickel. *Nat. Mater.* **6**, 740-743, doi:<https://doi.org/10.1038/nmat1985> (2007).
- 28 Boeglin, C. *et al.* Distinguishing the ultrafast dynamics of spin and orbital moments in solids. *Nature* **465**, 458-461, doi:<https://doi.org/10.1038/nature09070> (2010).
- 29 Carva, K., Legut, D. & Oppeneer, P. M. Influence of laser-excited electron distributions on the X-ray magnetic circular dichroism spectra: Implications for femtosecond demagnetization in Ni. *Europhys. Lett.* **86**, 57002, doi:10.1209/0295-5075/86/57002 (2009).
- 30 Zhukov, V. P., Chulkov, E. V. & Echenique, P. M. Lifetimes of Excited Electrons In Fe And Ni: First-Principles GW and the $\text{ST\$-Matrix}$ Theory. *Phys. Rev. Lett.* **93**, 096401, doi:<https://doi.org/10.1103/PhysRevLett.93.096401> (2004).
- 31 Zhukov, V. P., Chulkov, E. V. & Echenique, P. M. Lifetimes and inelastic mean free path of low-energy excited electrons in Fe, Ni, Pt, and Au: Ab initio $\text{\$}\mathrm{GW}\text{\$}+\text{\$}\mathrm{T}\text{\$}$ calculations. *Phys. Rev. B* **73**, 125105, doi:<https://doi.org/10.1103/PhysRevB.73.125105> (2006).
- 32 Bauer, M., Marienfeld, A. & Aeschlimann, M. Hot electron lifetimes in metals probed by time-resolved two-photon photoemission. *Prog. Surf. Sci.* **90**, 319-376, doi:<https://doi.org/10.1016/j.progsurf.2015.05.001> (2015).

- 33 La-O-Vorakiat, C. *et al.* Ultrafast Demagnetization Measurements Using Extreme Ultraviolet Light: Comparison of Electronic and Magnetic Contributions. *Phys. Rev. X* **2**, 011005, doi:<https://doi.org/10.1103/PhysRevX.2.011005> (2012).
- 34 Mathias, S. *et al.* Probing the timescale of the exchange interaction in a ferromagnetic alloy. *P. Natl. Acad. Sci. USA* **109**, 4792, doi:10.1073/pnas.1201371109 (2012).
- 35 Gort, R. *et al.* Early Stages of Ultrafast Spin Dynamics in a Fe_3Si Ferromagnet. *Phys. Rev. Lett.* **121**, 087206, doi:<https://doi.org/10.1103/PhysRevLett.121.087206> (2018).
- 36 (!!! INVALID CITATION !!! 16,36).
- 37 Shokeen, V. *et al.* Spin Flips versus Spin Transport in Nonthermal Electrons Excited by Ultrashort Optical Pulses in Transition Metals. *Phys. Rev. Lett.* **119**, 107203, doi:<https://doi.org/10.1103/PhysRevLett.119.107203> (2017).
- 38 Siegrist, F. *et al.* Light-wave dynamic control of magnetism. *Nature* **571**, 240-244, doi:<https://doi.org/10.1038/s41586-019-1333-x> (2019).
- 39 Zhukov, V. P. & Chulkov, E. V. The femtosecond dynamics of electrons in metals. *Phys. Usp.* **52**, 105-136, doi:<https://doi.org/10.3367/ufne.0179.200902a.0113> (2009).
- 40 Radu, I. *et al.* Ultrafast and Distinct Spin Dynamics in Magnetic Alloys. *Spin* **05**, 1550004, doi:<https://doi.org/10.1142/s2010324715500046> (2015).
- 41 <https://www.psi.ch/de/psd/scientific-highlights/athos-conceptual-design-report-cdr>

Supplementary Material: Simultaneous two-color snapshot view on ultrafast charge and spin dynamics in a Fe-Cu-Ni tri-layer

Benedikt Rösner,^{1*} Boris Vodungbo,² Valentin Chardonnet,² Florian Döring,¹ Vitaliy A. Guzenko,¹ Marcel Hennes,² Armin Kleibert,¹ Maxime Lebugle,¹ Jan Lüning,² Nicola Mahne,³ Aladine Merhe,² Denys Naumenko,³ Ivaylo P. Nikolov,³ Ignacio Lopez-Quintas,³ Emanuele Pedersoli,³ Primož R. Ribič,^{3,4} Tatiana Savchenko,¹ Benjamin Watts,¹ Marco Zangrando,³ Flavio Capotondi,³ Christian David¹, Emmanuelle Jal²

¹ Paul Scherrer Institut, 5232 Villigen PSI, Switzerland

² Sorbonne Université, CNRS, Laboratoire de Chimie Physique – Matière et Rayonnement, LCPMR, 75005 Paris, France

³ Elettra-Sincrotrone Trieste, Strada Statale 14-km 163,5, 34149 Basovizza, Trieste, Italy

⁴ Laboratory of Quantum Optics, University of Nova Gorica, 5001 Nova Gorica, Slovenia

Experimental geometry

The experiment was performed in the DiProI Ultra High Vacuum chamber of FERMI [[F. Capotondi *et al.* Journal of Synchrotron Radiation, 22 - 3, 544-552 \(2015\)](#)]. As represented in Figure S1 a), we used an x-y-z stage to position the twin-focus, off-axis zone plate, a sample x-y-z stage tilted for a 30° angle between the sample surface normal and the pre-zone plate beam propagation trajectory. With the set of parameters for the off-axis zone plates with an area of 3.8 mm x 3.8 mm, the resulting focal length is 74.4 mm, the spot displacement from the optical axis is 2.3 mm. A set of permanent magnets were set up around the sample to apply a field in the sample plane up to 130 mT in both directions. A CCD camera was placed approx. 220 mm downstream of the sample (resulting in a magnification of the projection of three) and

oriented for normal incidence of the 1st order beam from the twin-focus, off-axis zone plate in order to image the beam projection transmitted through the sample. Finally, the infrared (IR) pump laser beam was overlapped with the “sample” 1st order focus position of the twin-focus, off-axis zone plate on the sample tri-layer magnetic film with an angle of 10° with respect to the average beam trajectory of the zone plates 1st order focus. From the difference of the sample tilt and the diffraction angle of the XUV beam at the zone plate, we calculate an XUV incidence angle at the sample of 18° from the sample surface normal. Thus, the measured magnetization is equal to the real magnetization multiplied by $\sin(18^\circ)$ and the IR pump arrives with an incidence angle of 8° (Figure S1 b).

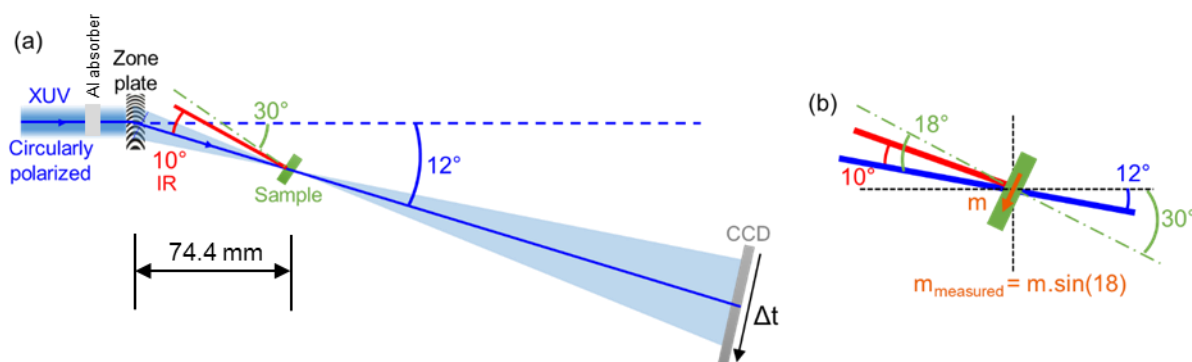


Figure S7 | Schematic illustration of the experimental geometry. a) Experimental scheme with angles between the sample surface normal and the incident XUV beam (green), between 1st zone plate diffraction order and incident XUV (blue), and between 1st zone plate diffraction order and incident IR pump (red). Note that the twin foci (pumped sample and unpumped reference spots, compare Figure 2 in main paper) are superimposed from this perspective. **b)** Zoom at the sample plane with representation of the in-plane magnetization of the metal tri-layer.

Normalizing data and retrieving XAS and XMCD absorption curves

As discussed in the main text, the twin-focus, off-axis zone plate projects two images onto the detector that correspond to photons coming from the two focus spots that illuminate the pumped sample area and

unpumped reference area of the tri-layer magnetic film. Figure S2 shows the raw and normalized data accumulated with 600 FEL shots, one applied magnetic field direction, and right-circularly polarized incoming XUV. Figure S2a shows the images recorded coinciding with IR pumping of the sample focus position (upper image; reference area shown in the lower image), while Figure S2b shows the respective images recorded without an IR pump pulse.

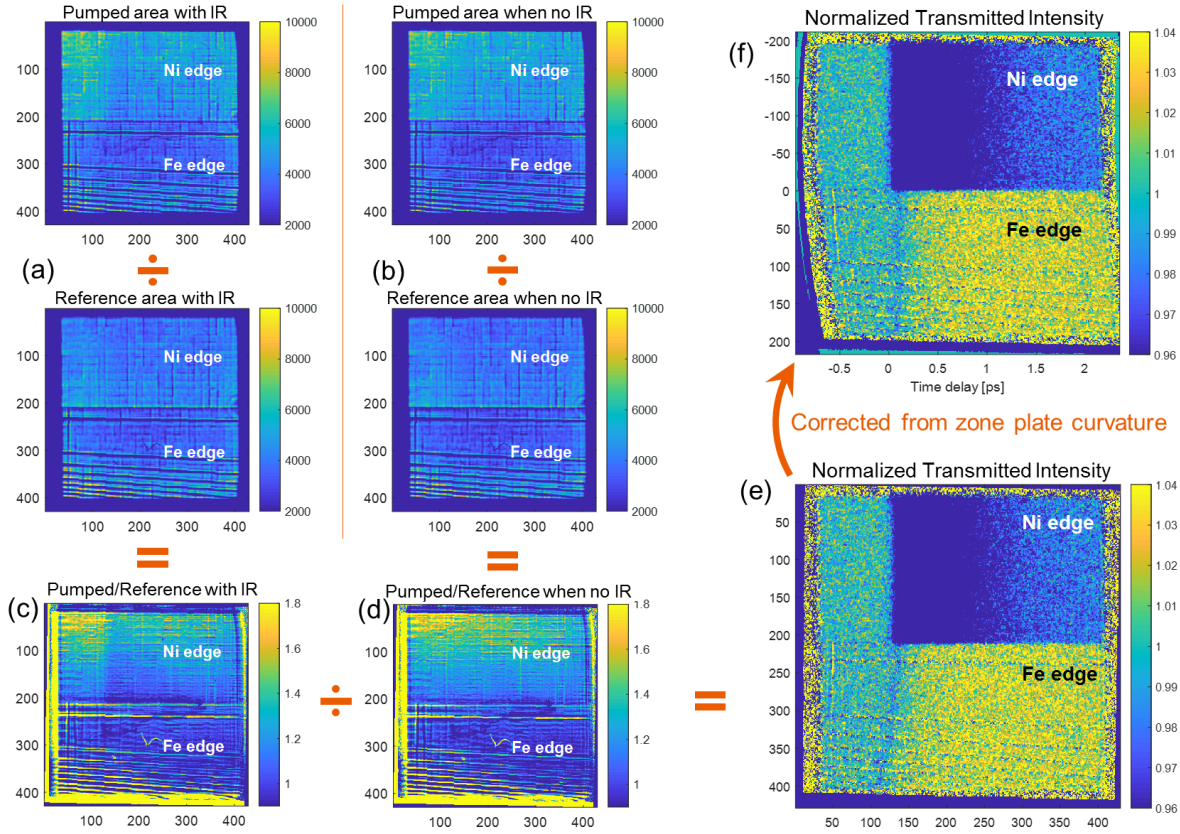


Figure S8 | Transmitted intensity of circularly right polarized XUV through the tri-layer Fe(10nm)/Cu(2nm)/Ni(10nm) for one applied field direction. a) Case for the two spots on the sample that are the pumped and reference areas with the IR pump switched on and b) for both spots without IR. Division of pumped area by the reference one for IR on (c) and IR off (d). e) Division of figure (c) and (d) to get the normalized transmitted intensity as explained in the text. f) Compensation of the zone plate curvature and an additional (linear) time streaking induced by the beam splitting. This is done by mapping the time information pixel by pixel calculating the path length to the focus spot from the respective area on the zone plate.

In general, the intensity recorded by the detector, I , can be broken down into contributions from the FEL source, I_0 , the optics and detector efficiency, η , and the interaction with the sample that follows the Beer-Lambert law [[A. Beer, Annalen der Physik und Chemie 86, 78-88 \(1852\)](#)]. In the case where the detector images have been corrected for tilts and curvatures, information about the time, t , and photon energy, E , are encoded into the x and y pixel-positions of the recorded images, respectively, to give:

$$I(S, x, y) = I_0(S, E(y)) \eta(E(y), x, y) e^{-\mu(E(y), t(x)) \cdot z} \quad (\text{eq. 1})$$

where S is the FEL shot index identifying the X-ray probe pulse, μ is the linear photoabsorption coefficient of the sample film and z its thickness. Each detector image contains regions corresponding to the sample and reference focus spot on the sample. Dividing these without providing a pump pulse gives the relative optics and detector efficiencies of the corresponding regions:

$$\begin{aligned} \frac{I_s(S_i, x_s, y_s)}{I_r(S_i, x_r, y_r)} &= \frac{I_0(S_i, E(y)) \eta(E(y), x_s, y_s) e^{-\mu_s(E(y)) \cdot z}}{I_0(S_i, E(y)) \eta(E(y), x_r, y_r) e^{-\mu_r(E(y)) \cdot z}} \\ &= \frac{\eta(E(y), x_s, y_s)}{\eta(E(y), x_r, y_r)} e^{-[\mu_s(E(y)) - \mu_r(E(y))] \cdot z} \end{aligned} \quad (\text{eq. 2})$$

where the s and r subscripts refer to the sample and reference detector image regions. To superimpose the two detector image areas, we used the Matlab `affine2d` function [<https://mathworks.com/help/images/ref/affine2d.html>], which mainly translates the image (besides a slight scaling to correct camera alignment errors) by a two-dimensional geometric transformation. Note that simultaneous measurement of the sample and reference positions allows equation 2 to cancel the shot-to-shot XUV intensity variations without an extra I_0 measurement, which can be challenging at Free Electron Lasers [[Higley et al., Rev. Sci. Instrum. 87, 033110 \(2016\)](#)].

Further, μ does not vary as a function of time without pumping and strong similarity between the magnetic film in the sample and reference focus positions should make the exponential term close to unity. The relative efficiency term is then expected to dominate the structures observed in this image ratio, which is shown in Figure S2d and appears to chiefly consist of three types of imperfections in the optical system: spatially inhomogeneous intensity distribution of the incident XUV pulse due an imperfectly flat wave front, inhomogeneities in the XUV diffraction efficiency of the twin-focus, off-axis zone plate, and stitching errors during the lithography step in the fabrication process of the twin-focus off-axis zone plate. If we now pump the material at the sample focus spot (indicating affected terms by an asterisk), we get:

$$\begin{aligned} \frac{I_s^*(S_i, x_s, y_s)}{I_r(S_i, x_r, y_r)} &= \frac{I_0(S_i, E(y)) \eta(E(y), x_s, y_s) e^{-\mu_s^*(E(y), t(x)) \cdot z}}{I_0(S_i, E(y)) \eta(E(y), x_r, y_r) e^{-\mu_r(E(y)) \cdot z}} \\ &= \frac{\eta(E(y), x_s, y_s)}{\eta(E(y), x_r, y_r)} e^{-[\mu_s^*(E(y), t(x)) - \mu_r(E(y))] \cdot z} \quad \text{(eq. 3)} \\ &\sim e^{-\Delta\mu(E(y), t(x)) \cdot z} \end{aligned}$$

Equation 3 says that taking the ratio of the pumped sample and reference regions of the detector image provides an approximate measure of the change in sample absorption as a function of time and energy encoded in the x and y pixel-positions. The precision of this normalization depends on the assumptions that the combined efficiency of the twin-focus, off-axis zone plate and the detector is trivial (*i.e.* equal to 1) and that the absorption coefficient of the material at the *sample* and *reference* focus positions are identical in the absence of pumping (*i.e.* $\mu_s = \mu_r$). This normalization is analogous to the “clean monitor” normalization method for TEY NEXAFS measurements described by Watts et al. [[Watts et al., J. Electron Spectrosc. Relat. Phenom. 151, 105-120 \(2006\)](#)] and is sufficient to observe some details of the dynamics as shown in Figure S2c.

However, the approximating assumptions in equation 3 can be removed by combining a pair of measurements from separate FEL shots (the i^{th} shot coinciding with a pump, the j^{th} not pumped) by dividing equation 3 by equation 2:

$$\begin{aligned} \frac{I_s^*(S_i, x_s, y_s)}{I_r(S_i, x_r, y_r)} \cdot \frac{I_r(S_j, x_r, y_r)}{I_s(S_j, x_s, y_s)} &= e^{-[\mu_s^*(E(y), t(x)) - \mu_s(E(y))] \cdot z} \\ &= e^{-\Delta\mu_s(E(y), t(x)) \cdot z} \end{aligned} \quad (\text{eq. 4})$$

This normalization is analogous to the “stable monitor” NEXAFS normalization method [[Watts et al., J. Electron Spectrosc. Relat. Phenom. 151, 105-120 \(2006\)](#)] that is based on the more reliable assumption that the relative efficiency and reference absorption terms (η and μ_r) are constant between shots. Figure S2e demonstrates that normalizing the data by the “stable monitor” method has removed the strong, nearly horizontal streaks from the image, flattening the left-hand, pre-IR-pump section of the image and bringing the system dynamics contrast well above the distortion and noise. A final correction of the image distortion caused by the curvature of the zone plate is applied by mapping each pixel to its respective time delay according to the local zone number [[Buzzi et al., Sci. Rep. 7, 7253 \(2017\)](#)] and the additional contribution to the path length by the beam splitting, see in Figure S2f and Figure 3 b) in the main text. From this figure and equation 4, we just need to integrate the two signals along the y-axis (the top part for Ni and the bottom part for Fe), perform the negative logarithm on this transmitted intensity ratio and divide by the corresponding sample layer thickness, z , to obtain the relative absorption as a function of the time delay, $\Delta\mu(t)$. Measuring the normalized transmitted intensity for the two directions of the magnetic field gives information on the two relative magnetic absorption spectra $\Delta\mu^{+/-}(t)$.

Figure S3 shows this relative magnetic absorption $\Delta\mu^{+/-}(t)$ for Ni and Fe. The error bars arise from the average of the curves measured with different experimental configuration (reversing the applied magnetic field or the circular XUV polarization). From these relative magnetic absorption spectra $\Delta\mu^{+/-}(t)$, the pure

relative absorption can be retrieved, which is sensitive solely to the electronic charge, $\Delta\text{XAS}(t) = \frac{\Delta\mu^+ + \Delta\mu^-}{2}$, and the relative XMCD signal, which is sensitive to the electronic spin, $\Delta\text{XMCD}(t) = \Delta\mu^+ - \Delta\mu^-$ (Figure 4 in the main text).

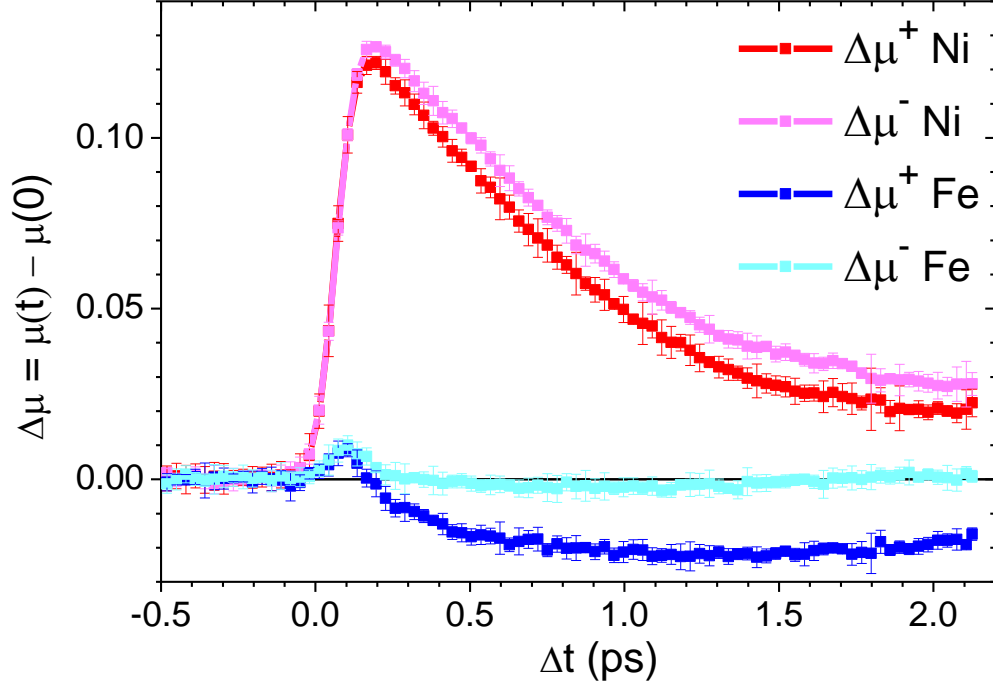


Figure S9 | Transient relative absorption for the two different direction of applied field for Ni and Fe.

Note that the normalized magnetization $\text{XMCD}(t)/\text{XMCD}(t < 0)$ is used in most studies, and not the relative form ΔXMCD . In our case, we do not have an absolute measurement of the incident XUV intensity I_0 , and thus cannot retrieve $\mu(t)/\mu(0)$ but only $\Delta\mu(t)$ and $\Delta\text{XMCD}(t)$. Division by $\text{XMCD}(t < 0)$ could result in minor changes in the relative demagnetization amplitude of Ni and Fe, but not in the time scales.

Fit parameters

To extract the time constant given in the main text, we fitted the $\Delta XMCD$ data by the equation derived by Malinowski et al. [[Malinowski et al., Nat. Phys. 4, 855 \(2008\)](#)]:

$$\Delta XMCD(t) = \left[\frac{-b}{\sqrt{t/d+1}} + \frac{ct_1-bt_2}{t_2-t_1} e^{-t/t_1} + \frac{t_2(b-c)}{t_2-t_1} e^{-t/t_2} \right] \Theta(t) \otimes \Gamma(t), \quad (\text{eq. 5})$$

where b is the amplitude after equilibrium, c is the initial electron temperature rise, d is the cooling by heat diffusion time (fixed to 50 ps), t_1 is the demagnetization time and t_2 is the recovery time. The Θ function is the Heaviside function, which we are convoluting by Γ , a Gaussian function with 120 fs full width at half maximum (FWHM) that accounts for the temporal resolution degradation corresponding to the mean squared duration of the XUV and IR pulses of 70 and 100 fs, respectively.

For the fitting of ΔXAS , we systematically screened constants b and c in equation 5. The parameters giving the fit shown in Figure 4 of the main text are summarized in the table below.

Table 1 | Fit parameters used in equation 5.

	b	c	t₁ (fs)	t₂ (ps)
D-XAS Fe	0.012	-0.02	30	0.2
D-XAS Ni	0	-0.13	38	1
D-XMCD Fe	0	0.02	500	5
D-XMCD Ni	0	0.01	240	5

Absorption profile

To quantify the IR absorption profile in our sample, we have calculated the attenuation of IR radiation using the transfer matrix method [<https://arxiv.org/abs/1603.02720>] and the “tmm” python software

package [<http://pypi.python.org/pypi/tmm>]. The optical constants are derived from the standard values provided by Palik [[Palik, Handbook of Optical Constants of Solids, Academic Press 1997](#)], listed in the table of Figure S4. The local absorption coefficient and integrated absorption through the different layers are shown in Figure S4.

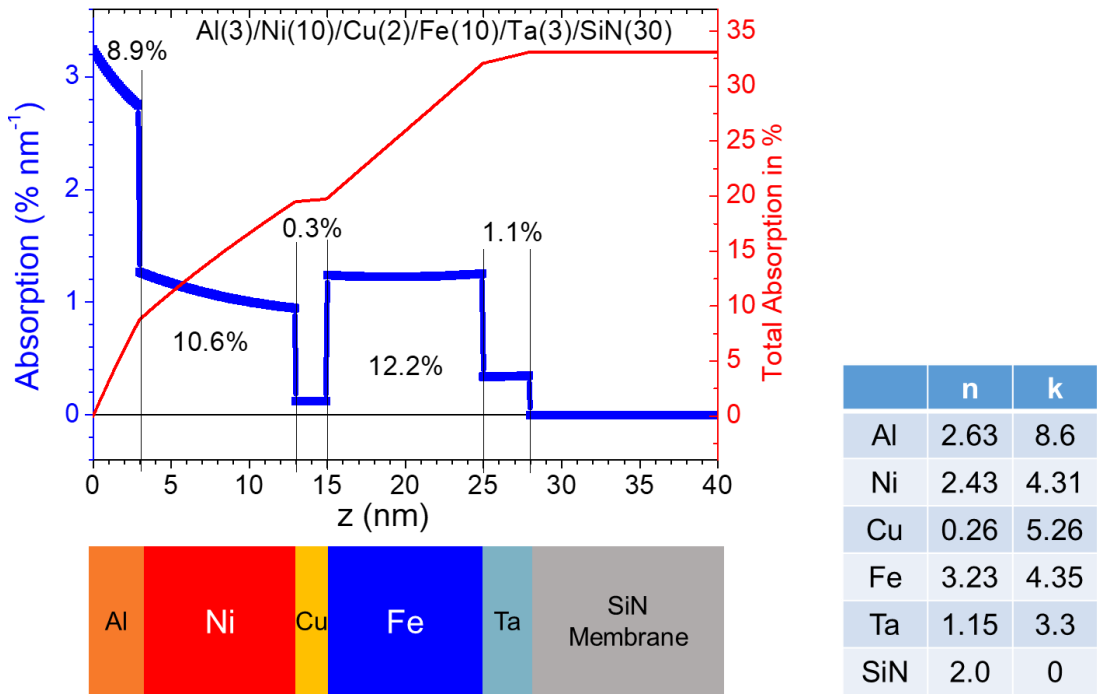


Figure S10 | IR absorption profile by our tri-layer samples. (blue) absorption rate in percentage per nanometer. (red) integration of the blue curve to demonstrate the total absorption at each layer (integral values for individual layers labelled on the graph in black).